

Geophysical Research Letters[®]



RESEARCH LETTER

10.1029/2024GL108206

Key Points:

- Fractures in glacier flow are modeled using material point method with elastoplasticity and tensile strain softening
- A dimensional analysis reveals a key dimensionless number characterizing two different regimes of fast fracture
- One regime predicts acknowledged ice tensile strength from field observations and characterizes the regular crevasse spacing

Supporting Information:

Supporting Information may be found in the online version of this article.

Correspondence to:

H. Rousseau,
hugo.rousseau@geo.uzh.ch

Citation:

Rousseau, H., Gaume, J., Blatny, L., & Lüthi, M. P. (2024). Transition between mechanical and geometric controls in glacier crevassing processes. *Geophysical Research Letters*, 51, e2024GL108206.
<https://doi.org/10.1029/2024GL108206>

Received 23 JAN 2024

Accepted 9 APR 2024

Corrected 24 MAY 2024

This article was corrected on 24 MAY 2024. See the end of the full text for details.

Author Contributions:

Conceptualization: Hugo Rousseau
Formal analysis: Hugo Rousseau
Methodology: Hugo Rousseau,
 Johan Gaume
Project administration: Martin P. Lüthi
Software: Lars Blatny
Supervision: Johan Gaume
Writing – original draft: Hugo Rousseau
Writing – review & editing:
 Hugo Rousseau, Johan Gaume,
 Lars Blatny, Martin P. Lüthi

© 2024. The Authors.

This is an open access article under the terms of the [Creative Commons Attribution-NonCommercial-NoDerivs License](#), which permits use and distribution in any medium, provided the original work is properly cited, the use is non-commercial and no modifications or adaptations are made.

Transition Between Mechanical and Geometric Controls in Glacier Crevassing Processes

Hugo Rousseau^{1,2} , Johan Gaume^{2,3,4} , Lars Blatny^{2,3,4} , and Martin P. Lüthi¹ 

¹Department of Geography, University of Zurich, Zurich, Switzerland, ²Institute for Geotechnical Engineering, ETH Zurich, Zurich, Switzerland, ³WSL Institute for Snow and Avalanche Research SLF, Davos, Switzerland, ⁴Climate Change, Extremes, and Natural Hazards in Alpine Regions Research Center CERC, Davos, Switzerland

Abstract Herein, fast fracture initiation in glacier ice is modeled using a Material Point Method and a simplified constitutive law describing tensile strain softening. Relying on a simple configuration where ice flows over a vertical step, crevasse patterns emerge and are consistent with previous observations reported in the literature. The model's few parameters allows identification of a single dimensionless number controlling fracture spacing and depth. This scaling law delineates two regimes. In the first one, ice thickness does not play a role and only ice tensile strength controls the spacing, giving rise to numerous surface crevasses, as observed in crevasse fields. In this regime, scaling can recover classical values for ice tensile strength from macroscopic field observations. The second regime, governed by ice bending, produces large-scale, deep fractures resembling serac falls or calving events.

Plain Language Summary In ice sheets and alpine glaciers, fast-flowing sections are often characterized by crevasse fields that play a significant role in the cryo-hydrologic system by facilitating meltwater flow, enhancing basal sliding, weakening the ice, and impacting glacier thermodynamics. Modeling these fractures at the glacier scale remains challenging and often necessitates integrating diverse models which hinders the straightforward consideration of physical issues associated with crevasse fields on a large scale. Here, a new numerical framework allows us to conduct field-scale experiments and paves the way for a scaling law to elucidate the macroscopic factors influencing fracture fields and to easily incorporate crevasse depth and spacing into large-scale models. A newly discovered scaling law highlights the transition between a mechanical behavior where the regular crevasse spacing is unaffected by geometry to a regime where geometry plays a significant role, particularly in large-scale fracture processes like glacier calving. While the numerical experiments in this paper focus on glaciers, the model and conceptual framework is versatile and can address the mechanical behavior of fractures in broader geophysical contexts such as snow, rock or ice avalanches, tectonics and landslides.

1. Introduction

Fractures are hallmark features of rapidly flowing glaciers. Ocean-terminating outlet glaciers of the ice sheets release large volumes of ice into the ocean by fracturing processes, termed glacier calving. Large inland areas of the ice sheet also exhibit highly crevassed zones which form integral components of the cryo-hydrologic system, (Chudley et al., 2021; Kozlo & Arnold, 2018; McGrath et al., 2011; Phillips et al., 2010) by storing meltwater and facilitating pathways to the glacier bed, ultimately affecting basal sliding (Andrews et al., 2014; Schoof, 2010; Sole et al., 2011) and hence the glacier dynamics. While these processes demonstrate the need to consider crevasses in glacier simulations, accurately modeling and comprehending the varied characteristics of these fractures remains challenging. For instance, in crevasse fields, Holdsworth (1969) observed that despite different ice temperatures and strain rates, the spacings between initial transverse crevasses were surprisingly similar, with variations ranging from 57 to 66 m for cold ice. Such order of magnitude was later recovered in different glaciers with different configurations (Enderlin & Bartholomäus, 2020; Garvin & Williams, 1993; Malthe-Sørensen et al., 1999); however, slightly smaller values were also observed on the lower part of Jakobshavn Isbræ, with values ranging from 20 to 40 m (Garvin & Williams, 1993), and on the Western Skaftá cauldron collapse in Iceland (Malthe-Sørensen et al., 1999). Moreover, Weiss (2003) suggested that crevasses are more regularly spaced than would be expected from a random process, and thus, contrary to what is classically observed for icebergs resulting from calving events, do not exhibit a fractal distribution (Walter et al., 2020).

In an attempt to explain regular crevasse spacing, Nielsen (1958) proposed a simple mechanism based on a flowing cantilever ice slab passing over a bedrock jump where fractures appear when the ice weight becomes excessive. In this approach, crevasse spacing is a function of ice thickness and tensile strength. This result was discussed by Holdsworth (1969), who showed that it worked only in limited cases and argued that crevasse spacing should not depend on ice thickness.

The modeling of crevasse depth has received considerable attention since Nye (1955, 1957) introduced a theory for closely spaced crevasses in an infinite slab of ice arguing that crevasses propagate downward when longitudinal stress exceeds overburden pressure. Although the theory agrees well with field observations at the first order (Enderlin & Bartholomäus, 2020; Holdsworth, 1969; Mottram & Benn, 2009), it is limited to uniform crevasse fields because the stress singularities at crevasse tips are negligible in this case (van der Veen, 1998; Duddu et al., 2020). To address this issue, linear elastic fracture mechanics (LEFM) proposes that mode I fractures form under tension at short timescales as long as the stress intensity factor acting on an initial crack is higher than the fracture toughness of the ice (Smith, 1976; Weertman, 1977; van der Veen, 1998; van der Veen, 2007). Within this framework, the maximum crevasse depth depends on the ice thickness through a weight function in the stress intensity factor (van der Veen, 1998). However, such functions are largely dependent on crevasse configuration (Jiménez & Duddu, 2018), and their derivation is far from trivial. Another limitation is related to the purely elastic approach that disregards plastic deformation and overestimates the stress concentration at the crack tip. Moreover, LEFM only predicts the vertical propagation of small initial cracks introduced as the starting condition. Thus, crevasse spacing is an input parameter that must be properly accounted for to provide better results than those of the model of Nye (1957) (Mottram & Benn, 2009). The initial cracks are modeled using continuum damage mechanics (CDM), where a damage state variable is advected by the ice flow (Duddu & Waisman, 2013; Huth et al., 2021a; Pralong et al., 2003; Pralong & Funk, 2005) to represent small defects in the ice. This approach was coupled with LEFM by Krug et al. (2014) to simulate the calving of ice and provide realistic results. However, an additional damage equation must be solved, demanding additional parameters to be determined using field data.

Alternative approaches have been based on discrete element modeling (DEM). This approach escapes the continuum representation of fractures and therefore directly reproduces realistic patterns (Bassis & Jacobs, 2013) and the fractal nature of icebergs (Åström et al., 2014). Nevertheless, these simulations are computationally very expensive.

More recently, Wolper et al. (2021) proposed a continuum damage material point method (MPM) associated with elastoplasticity for glacier calving and tsunami genesis. The Eulerian–Lagrangian description of the MPM allowed for the emergence of realistic fracture patterns while relying on continuum equations to reduce computational time. Herein, we used the same framework but with a simpler elastoplastic law associated with strain softening, thus reducing the number of parameters while maintaining the essence of the previous model. The spacing and depth of the crevasses appear naturally with a simulation duration of a reasonable amount of time, which allows us to perform dimensional analysis on all key parameters to isolate the mechanisms behind the rapid formation of crevasses. A single dimensionless number drives these fractures with a regime that explains the regular spacing of the crevasses in agreement with the intuition of Holdsworth (1969). The scaling law also facilitates the comparison of the model using field data and establishes a connection between field observations and crucial parameters. Relying on such scaling law provides a more straightforward approach within broader frameworks. Its development would facilitate coupling with large-scale models to integrate crevasse spacing and depths, while considering the local geometric and mechanical parameters of the ice. For instance, this could help accounting more easily for crevasses to study and model the cryo-hydrologic system.

2. Method

To deal with large inelastic deformations in a continuum framework, our numerical approach relies on MPM (Sulsky et al., 1994), in which we implement a finite strain elastoplastic constitutive model (Gaume et al., 2018; Klár et al., 2016; Mast, 2013; Simo, 1992). In such models, a yield function Φ defines elastic states $\Phi < 0$ and the yield surface $\Phi = 0$ where plastic deformations occur. Here, we consider a capped strain-softening von Mises yield function, which allows tensile fractures, such as calving and transverse crevasses, in glaciers (Colgan et al., 2016; Krug et al., 2014; Weiss, 2003) to be addressed by considering such events as brittle, particularly in the form of strong softening after failure. The yield function is given by

$$\Phi(p, q) = \begin{cases} q - q_y & \text{if } p > p_c(\zeta, \epsilon_v^p) \\ p - p_c(\zeta, \epsilon_v^p) & \text{otherwise,} \end{cases} \quad (1)$$

where the pressure is $p = -\frac{1}{d}\text{tr}(\boldsymbol{\sigma})$ and the equivalent von Mises stress is $q = \sqrt{\frac{3}{2}\text{dev}(\boldsymbol{\sigma}) : \text{dev}(\boldsymbol{\sigma})}$, where d is the space dimension and $\boldsymbol{\sigma}$ the Kirchhoff stress using $\text{dev}(\boldsymbol{\sigma})$ to denote deviatoric stress. A tensile cap p_c on the von Mises yield surface allows failure under tension to be considered. This model implies that for a state of stress where $p > p_c$, plastic deformation develops with a shear strength q_y through an associative flow rule inducing no compaction/dilatancy. However, we allow volumetric plastic expansion for states under tension at $p = p_c$, thus increasing the accumulated volumetric plastic strain ϵ_v^p . The cap depends on ϵ_v^p , particularly $p_c = p_c(\zeta, \epsilon_v^p) = -ce^{-\zeta\epsilon_v^p}$, where $c > 0$ is the cohesion (or tensile strength) of the undamaged material and $\zeta > 0$ gives the degree of postyield softening. Thus, initially, $p_c = -c$, then with accumulating volumetric plastic strain, p_c increases toward zero naturally leading to material separation (Blatny et al., 2021, 2023; Klár et al., 2016; Stomakhin et al., 2013; Wolper et al., 2019, 2021). For more details on the numerical scheme and the elastoplastic law, please refer Supporting Information S1.

Because there is no viscosity in the model, we restricted our study to brittle and rate-independent fractures occurring at very short timescales and large strain rates. Therefore, we do not expect the model to reproduce the full complexity of the stress field but rather to highlight potential rate-independent structures that can emerge. We assume that this scenario is likely for ice passing over a bedrock step. The configuration is sketched in Figure 1a, where H_i is the glacier thickness, L_s is the slope length, H_s is the height of the slope, W_i is the glacier width, $\rho_i = 917 \text{ kg m}^{-3}$ is the ice density, and g is the gravity. The Young's modulus E is set to 1 GPa and the mesh size to $dx = 10 \text{ m}$. To remove mesh sensitivity introduced by the softening law, we followed the same approach as Gaume et al. (2018) and Kohler et al. (2022) by adjusting the softening factor ζ with dx such that the same amount of energy is dissipated regardless of the mesh size.

A Coulomb friction law was applied at the base of the glacier, and a frictionless condition was applied on the lateral sides. This allowed us to avoid fractures generated by side friction and isolate the fracture processes induced by the break of the slope. The glacier flow was simulated using a constant velocity $V_x = 4 \text{ m s}^{-1}$ imposed at its back. We checked that the velocity does not affect the results (Figure S2 and Text T1 in Supporting Information S1). Other parameters of the simulations can be found in Table S1 in Supporting Information S1.

3. Results

The result of a three-dimensional (3D) simulation, corresponding to Figure 1a is presented in Figure 1b (Movie S1). Numerous fractures, that are regularly spaced, emerged and, despite the purely elastoplastic framework, showed great similarity to the crevasse patterns of a glacier flowing over bedrock steps (Figure 1c).

By calling the intercrevass spacing L_p , a parametric study was conducted to determine the mechanical and geometrical properties driving the spacing and depth.

3.1. Dimensional Analysis of Crevasse Spacing

We assumed that the spacing between crevasses was controlled by five dimensionless numbers such that

$$\frac{L_p}{H_i} \propto \mathcal{F}\left(\frac{W_i}{H_i}, S, \frac{L_s}{H_i}, \frac{c}{\rho_i g H_i}\right), \quad (2)$$

where $S = H_s/L_s$ is the bedrock slope of the step. The role of bottom friction is left for further studies. Henceforth, the number $c/\rho_i g H_i$ is called the dimensionless cohesion. In Figure 2a, the median dimensionless spacing between crevasses \hat{L}_p/H_i is plotted as a function of this number. The analysis is performed for two-dimensional (2D) simulations to model a long glacier and to obtain a large number of crevasses. In this figure, the data gathered around two different regimes described by two different power laws of the dimensionless cohesion. In the upper area, the black dotted line has a slope of 0.5, which implies that

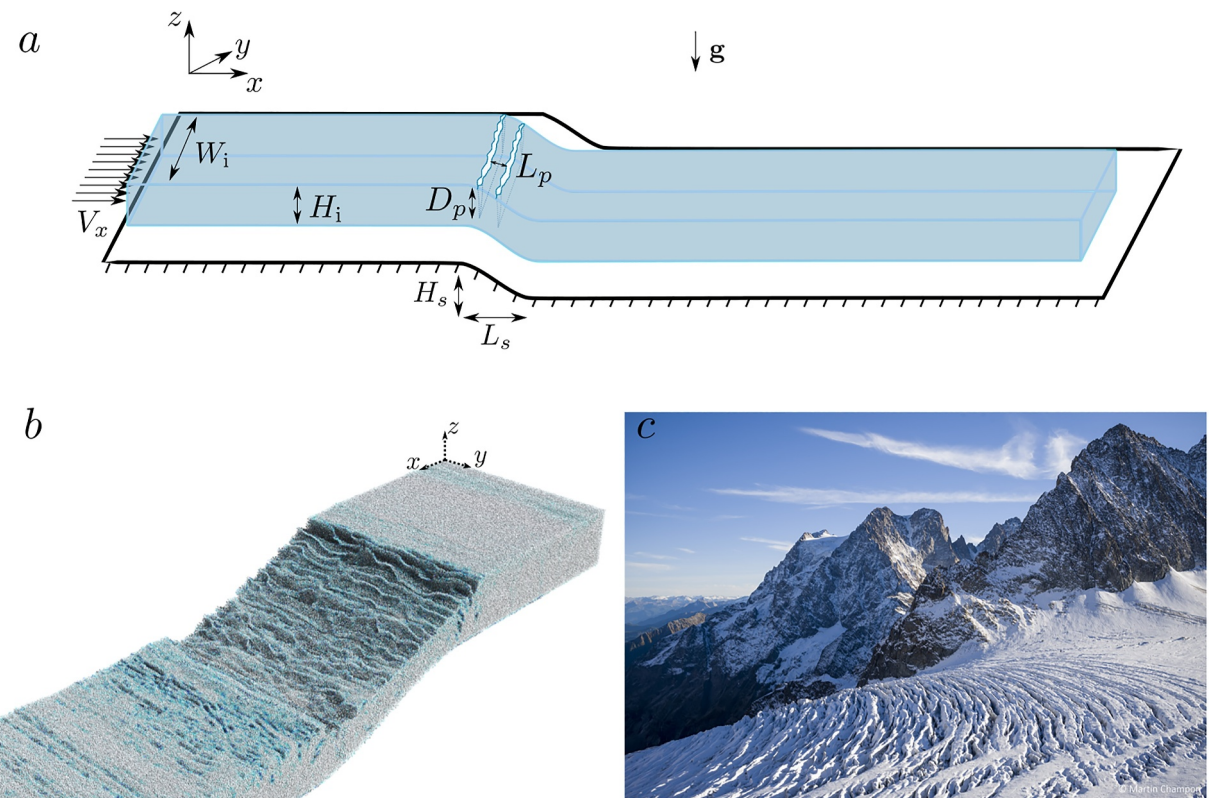


Figure 1. (a) Sketch of the modeled configuration. Please note that there are no crevasses present at the initial timestep. (b) Snapshot of MPM simulation results. (c) Glacier Blanc, French Alps. Credit: Martin Champon.

$$\hat{L}_p = \xi_1 \left(\frac{cH_i}{\rho_i g} \right)^{0.5} = L_b, \quad (3)$$

where ξ_1 is a constant. This dependency scales with the so-called bending length L_b (Petrenko & Whitworth, 1999; Wolper et al., 2021), which is required to fracture a cantilever beam of tensile strength c . This implies that in this regime, the median length between crevasses is controlled by the geometrical bending law proposed by Nielsen (1958).

In the lower regime (gray dotted line), linear dependency with dimensionless cohesion implies the following relation:

$$\hat{L}_p = \xi_2 \frac{c}{\rho_i g}, \quad (4)$$

where ξ_2 is a constant. In this regime, the spacing is given by characteristic length for which the hydrostatic stress equals the tensile strength. Such a length scale was considered a driving parameter for cohesive granular collapse (Gans et al., 2023). In addition, this suggests that the glacier thickness does not impact the spacing between crevasses in this regime (we verified in Figure S3 in Supporting Information S1 that the ratio L_s/H_i does not impact the spacing in this regime either). Therefore, the fractures are only controlled by the mechanical properties of the ice; thus, we call this behavior the mechanical regime. By increasing the ice cohesion from 15% to 30 % of the overburden stress, the geometry starts to influence the intercrevasse spacing as we enter the geometrical bending regime.

In Figure 2a, the red empty markers represent the results obtained from 3D simulations. These points also scale with the identified regimes, showing that the width W_i can be excluded from the analysis. This was expected because a free slip boundary condition was used on the lateral sides.

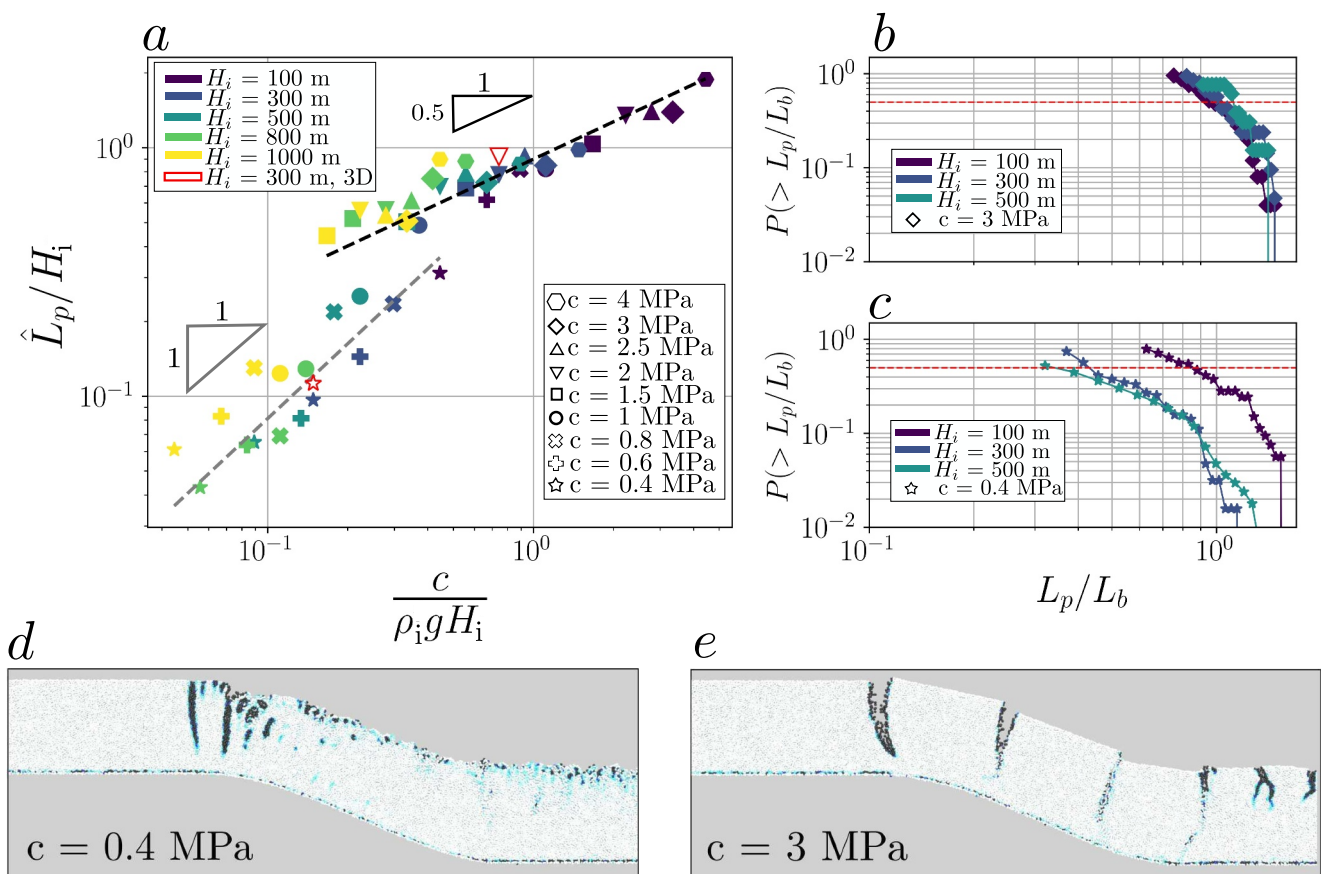


Figure 2. (a) Median dimensionless average distance between crevasses \hat{L}_p/H_i as a function of dimensionless cohesion $c/(\rho_i g H_i)$. (b) Cumulative distribution of intercrevasse spacing for three simulations in the geometrical bending regime. (c) Cumulative distribution of intercrevasse spacing for three simulations in the mechanical regime. Snapshots of 2D simulations corresponding to (d) the mechanical regime (see Movie S2) and (e) the geometrical bending regime (see Movie S3). The darker the color, the higher the volumetric plastic deformation ϵ_v^p .

To characterize crevasse spacing distribution, the cumulative distributions are illustrated in Figures 2b and 2c for different simulations. These distances are normalized by the bending length L_b (Equation 3) for the simulation parameters. For clarity, we showed only three simulations per figure; however, the distributions from other simulations exhibited the same behavior. Figure 2b shows the distribution of the simulations that fit the geometrical regime in Figure 2a. The distributions are sharp with values close to the median (red dotted line in Figures 2b and 2c). Figure 2c shows the distribution of simulations that pertain to the mechanical regime in Figure 2a. Data points corresponding to a distance $L_p < 30$ m were removed to avoid bias in our results owing to the mesh size of $dx = 10$ m. In this case, the distributions were larger than those for the geometrical regime, with the median indicating that 50% of the data points fell below $L_p/L_b = 0.3$ (with the exception of the scenario where $H_i = 100$ m, which was almost in the geometrical regime). This illustrates that a different regime distinct from the geometrical regime is indeed at play. Despite this variability in crevasse spacing, the median intercrevasse spacing in Figure 2a seemingly agrees well with the deterministic law provided by Equation 4.

3.2. Dimensional Analysis of Crevasse Depth

Figures 2d and 2e shows snapshots corresponding to the mechanical and geometrical regimes. A difference in the crevassing structure is clearly apparent. For the mechanical regime, numerous crevasses with various depths are observed. By contrast, in the geometrical regime, crevasses are always deep and clearly separated. To determine whether a characteristic depth associated with each regime exists, the normalized median crevasse depth \hat{D}_p/H_i was plotted as a function of dimensionless cohesion. In Figure 3a, the purple vertical strip denotes the transition

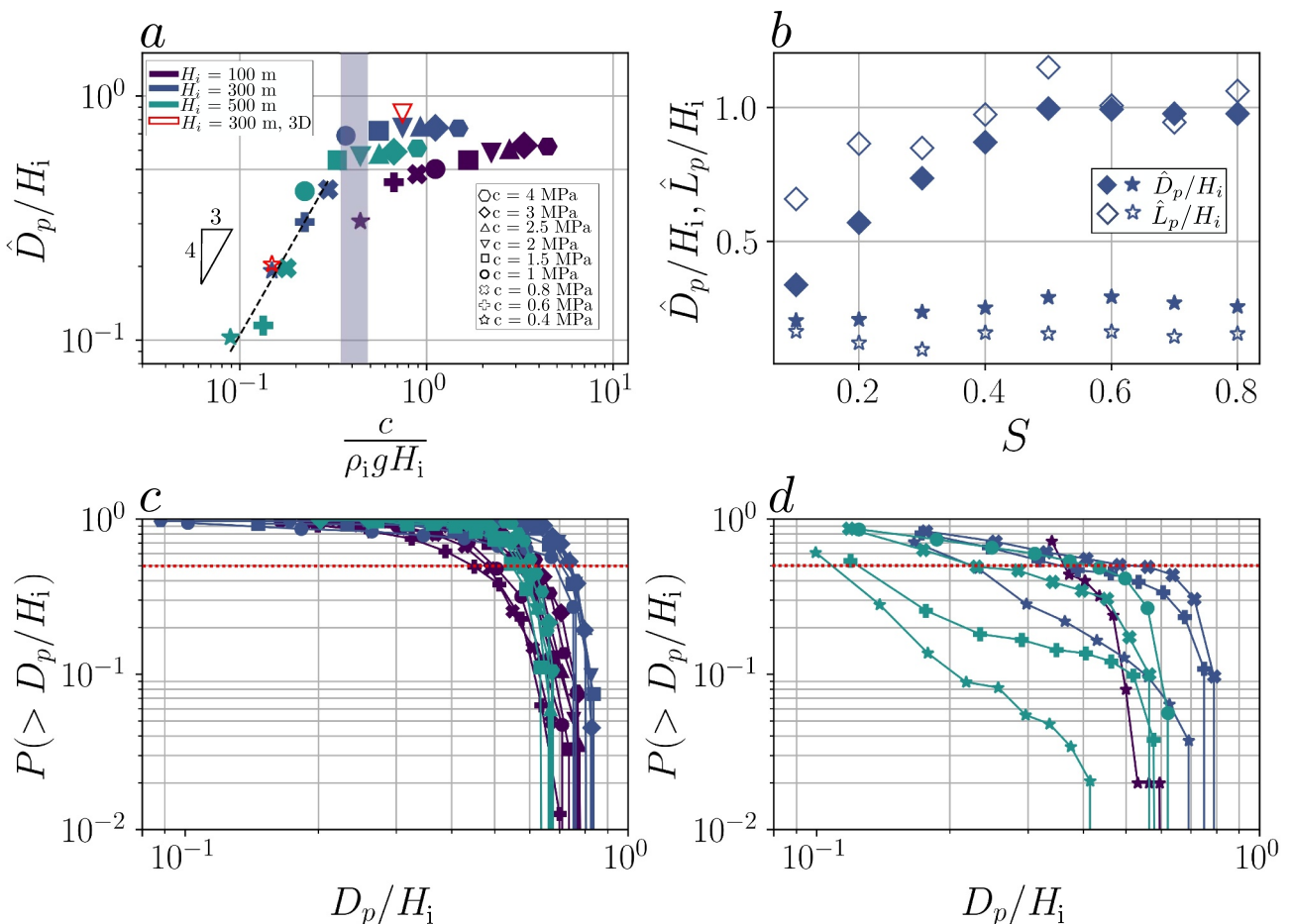


Figure 3. (a) Median dimensionless depth of crevasses as a function of dimensionless cohesion. (b) Median dimensionless depth of crevasses and median dimensionless intercrevasse spacing as a function of the slope of step S . (c) Cumulative distribution of crevasse depths presented in panel 3a for the points in the geometrical regime. (d) Cumulative distribution of crevasse depths in panel 3a for the points in the mechanical regime.

between the two behaviors identified in the previous section. For clarity, the analysis is limited to the ice thicknesses below 800 m.

In the geometrical regime, Figure 3a shows that the median normalized crevasse depths are always deeper than half of the ice thickness and are of the same order regardless of the parameters (with a slight shift for $H_i = 100$ m as, in this case, the regime is close to the fully geometrical behavior). Figure 3b shows how the median depth varies with the slope of the step. For the geometrical regime ($c = 3$ MPa and $H_i = 300$ m), the median depth \hat{D}_p is always higher than that in the mechanical regime for all slopes higher than $S = 0.2$ and reaches half of the glacier thickness. For slopes exceeding $S = 0.5$, the fractures penetrate the entire glacier thickness. Moreover, the crevasse depth distribution in Figure 3c suggests that the crevasse depths have a very sharp distribution with values always of the same order for this regime, indicating that only deep fractures are involved. These results allowed us to conclude that above the bed slopes of 0.2, deep fractures that involved more than half of the glacier thickness were characteristic of the geometrical regime.

Figure 3a also shows that in the mechanical regime, the median normalized crevasse depth is always lower than half of the glacier thickness and follows the power law of dimensionless cohesion with

$$\hat{D}_p = \xi_3 \left(\frac{c}{\rho_i g H_i} \right)^{4/3} = \frac{\xi_3}{H_i^{1/3}} \left(\frac{c}{\rho_i g} \right)^{4/3}. \quad (5)$$

The right-hand-side formulation is reminiscent of zero-stress model except that we obtain a power law slightly higher than unity. In addition, the term $c/\rho_i g$ is proportional to crevasse spacing through Equation 4, which shows that we recover the same behavior predicted by LEFM (van der Veen, 1998): a decrease in $c/\rho_i g$ leads to small crevasse spacing and a decrease in crevasse depth. However, in Equation 5, the inverse dependency was because of the step. For a given length of the step, the tensile stress generated by the change at the glacier base propagated less into the ice column for a thicker glacier. A similar behavior was observed by Zhang et al. (2023) using LEFM. They observed that for a disturbance on the ground, the ratio between the length of the disturbance and the ice thickness of the glacier L_s/H_i had an impact on the depth of a basal crevasse. In our configuration and contrary to the intercrevasse spacing, this ratio also impacted the crevasse depth, with crevasses becoming shallower as the ratio increased (Figure S3 in Supporting Information S1).

Figure 3d shows the crevasse depth distribution for the mechanical regime. Despite the majority of small crevasses ($D_p/H_i < 0.3\text{--}0.4$), the distributions were large and crevasses involving more than half of the thickness (i.e., characteristic of the geometrical regime) were still present (about 10%). This means that the bending mechanism can remain in the mechanical regime. In Figure 3b, the slope dependence for the mechanical regime (points marked with stars) shows that the median crevasse spacing and depth are almost insensitive to slope variations. This supports the idea that the spacing between crevasses is purely driven by the mechanical properties of the ice and is independent of its geometry. Nevertheless, because the geometrical regime still persists in the mechanical regime, the maximum crevasse depth observed in the mechanical regime follows the same dependency with the slope as the mean crevasse depth in the geometrical regime (Figure S4 in Supporting Information S1). This means that only small crevasses are unaffected by slope variations. Numerous crevasses mask the slope dependency of the few large crevasses.

In the mechanical regime, median crevasse depths were between 50 and 200 m, which were higher than that generally observed in the field, where values generally range from a few meters to 70–80 m (Herzfeld et al., 2021; Holdsworth, 1969; Mottram & Benn, 2009). A possible explanation is that we determined the crevasse depth using the volumetric plastic deformation e_v^p . Therefore, our quantification considered microfractures appearing below the open portion of the crevasses; thus, the depths were overestimated compared with field measurements.

4. Discussion

In this section, the obtained scaling relations are discussed with respect to field observations. Considering crevasse spacing, the cases of the Eastern and Western Skáftá cauldron collapses in the Western Vatnajökull ice cap (Iceland) were investigated. These collapses, induced by episodic subglacial drainages (Figure 4a), have been well studied, providing data for the spacing between crevasses (Malthe-Sorensen et al., 1999) and additional parameters such as ice thickness (Jóhannesson et al., 2007; Ultee et al., 2020) or the mechanical properties of ice (Ultee et al., 2020). The configuration was slightly different from that of a glacier flowing over a step; however, crevasses rapidly formed owing to tensile stress caused by rapid subsidence of the basal ground (leading to a similar shape of the ground). To investigate this geometrical setting, we simulated a glacier flowing over a concave step in Figure 4b. The results show qualitatively similar shapes and crevasse patterns as in the case of subglacial drainage, as shown in Figure 4a.

The distribution of crevasse spacings from the western cauldron is shown in Figure 4c (Malthe-Sorensen et al., 1999), exhibiting a median value $\hat{L}_p \sim 19$ m. At this location, the ice thickness was about $H_i = 300$ m, which gives $\hat{L}_p/H_i \sim 0.07$ (Jóhannesson et al., 2007; Ultee et al., 2020). From Figure 3a, such a ratio should correspond to the mechanical regime with a dimensionless cohesion equal to 0.08; that is, the cohesion would be $c = 0.20$ MPa.

The complex interplay between the development of fractures at viscous timescales and fast cracks during elastic relaxation times is an open issue in glacier physics (Weiss, 2019). On the one hand, Ultee et al. (2020) considered viscoelastic deformations and found that the tensile strength should be around 1 MPa, which is five times higher than that suggested by our model. With $c = 1$ MPa, the dimensionless cohesion would be 0.37 and would correspond to $L_p/H_i \sim 0.4$, giving a characteristic spacing of about 120 m, which is six times higher than that observed on the cauldron. On the other hand, several studies have suggested a low threshold in the range of 0.04–0.32 MPa for in situ observations (Vaughan, 1995; van der Veen, 1999) or between 0.10 and 0.50 MPa for models based on CDM or DEM, where fractures initiate at short timescales (Duddu & Waisman, 2013; Krug et al., 2014;

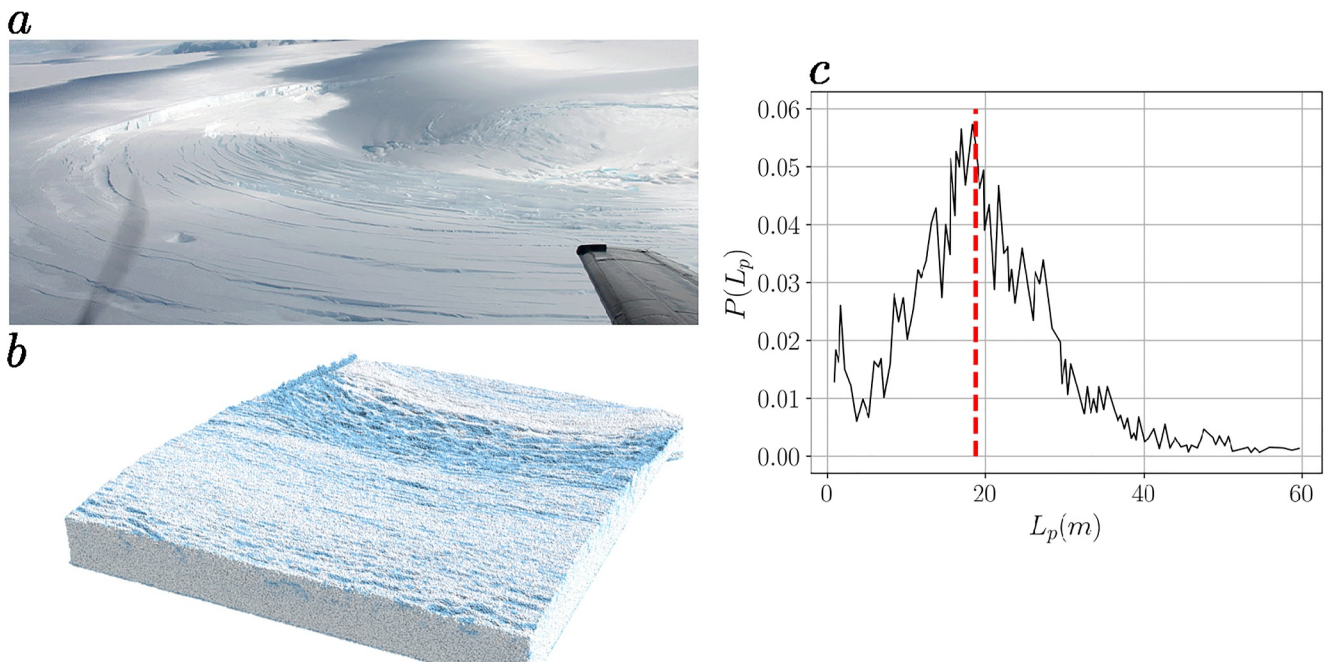


Figure 4. (a) Image of eastern Skaftá cauldron in Vatnajökull ice cap, Iceland (Magnússon et al., 2021). (b) MPM simulation of a glacier flowing over a concave step. (c) Size distribution of the spacing between crevasses of the Skaftá cauldron (from Malthe-Sorensen et al. (1999)). The red-dashed line represents the median value.

Pralong & Funk, 2005; Åström et al., 2013, 2014). Such values indicate a cohesion of $c = 0.20$ MPa and suggests, in this case, that our scaling law can provide realistic values for crevasse spacing. As the spacing is driven by the mechanical regime, such a crevasse formation does not depend on geometrical properties such as glacier thickness or bedrock slope (Equation 4). Such an idea was proposed by Holdsworth (1969), who argued that bending could not be responsible for the regular spacing between crevasses. Lastly, we should mention that our scaling does not address viscous timescales; therefore, we do not expect it to accurately reproduce the entire crevasse field or strain field.

Movie S4 shows the icefall of the Trift glacier in Switzerland. The configuration is similar to the one proposed in this study because it features an abrupt change in the slope. In this movie, a large and deep fracture regularly appears at the break of the slope, similarly to Movie S5, which shows geometrical fractures. In this way bending could be involved in such serac formations. Our scaling suggests, in this case, two possibilities. If the glacier thickness is very low, the dimensionless cohesion is sufficiently high such that the glacier fractures are purely driven by the geometrical regime; that is, no small fractures should develop. By contrast, if the dimensionless cohesion indicates rather the mechanical regime, small fractures should also develop as both types of fractures can coexist in this regime. The presence of small fractures advocate for the second option; however, this should be taken cautiously as other mechanisms besides brittle fractures could cause this smaller fractures.

A certain class of calving events could likely be analyzed within the same framework. Wolper et al. (2021) showed that the size of initial icebergs from calving events could be given by

$$\frac{L_p}{H_i} = \mathcal{F} \left(\frac{c}{\rho_i g H_i} \frac{1}{|1 - \frac{\rho_w D}{\rho_i H_i}|} \right), \quad (6)$$

with ρ_w as the water density, D as the depth of the immersed ice, and $\rho_w/\rho_i \sim 0.9$. In this law, we recovered dimensionless cohesion with a factor $1/|1 - \frac{\rho_w D}{\rho_i H_i}|$ accounting for buoyancy. This factor strongly increased the dimensionless cohesion as the ratio D/H_i tended to 0.9 at full buoyancy (Wolper et al., 2021). This shows that the

effect of sea water is the shifting of the dimensionless cohesion to high values where only the geometry drives the fractures. By contrast, without seawater, the mechanical regime could be the driving regime. Equation 6 also shows that if the glacier can reach full buoyancy ($D/H_i = 0.9$), the length of the icebergs becomes infinite so that no fractures can appear because of ice bending. However, although this observation could explain certain large calving events, it does not explain small calving events or the fractal distribution of icebergs (Walter et al., 2020; Weiss, 2003). Further research should be performed to determine how our scaling relates to the distribution observed by Åström et al. (2021) for instance. Damaged ice and viscous deformation at calving face could induce small fractures. Also, other fracture processes exist in shearing mode such as the crushing and grinding of icebergs (Åström et al., 2014, 2021).

5. Conclusion

We presented a new approach that comprises solving an elastoplastic law with tensile strain softening using MPM. The major advantage of MPM is its explicit simulation of damage and fracture emergence during the glacier flow. Based on the model results, we performed a dimensional analysis highlighting two distinct regimes that control the spacing and depth of the fractures and are governed by a single ratio between cohesion and hydrostatic stress. The first regime controls the regular spacing of crevasses observable on a glacier, whereas the second regime is involved in large serac falls and calving events. Relying on this dimensionless number allowed us to identify the different mechanisms behind brittle crevasses. In addition, the scaling law driven by this dimensionless number hints to a ice tensile strength of 0.2 MPa (a value acknowledged in the literature), demonstrating its potential capacity to match field observations. We believe that such scaling laws would allow for straightforward comprehension and implementation of fractures on glaciers but also more generally for patterns in snow science, tectonics and landslides. However, the purely elastoplastic framework cannot capture the viscous nature of ice flow over long timescales. Further investigation is needed to clarify the role of viscosity in the observed mechanisms in order to propose a more comprehensive scaling law. This could yield insights to evaluate the utility of elasto-(visco)plastic models in glacier modeling. Another perspective would be to develop a shallow-shelf approximation of this model to address efficiently large scale geometries such as proposed by Huth et al. (2021b) and Guillet et al. (2023). Lastly, the model presented here can be used or extended easily to model fracture processes in a broader spectrum of earth science applications, particularly for snow, rock or ice avalanches, tectonics and landslides.

Data Availability Statement

Data and codes used in this work are freely available from Zenodo (Rousseau et al., 2024).

Acknowledgments

This study was supported by the Swiss National Science Foundation (SNSF) project COEBELI (Grant 200.020_197015/1). We also thank Prof. em. Dr. Martin Funk for providing the movie of the Trift glacier.

References

- Andrews, L., Catania, G., Hoffman, M., Gulley, J., Lüthi, M., Ryser, C., et al. (2014). Direct observations of evolving subglacial drainage beneath the Greenland Ice Sheet. *Nature*, 514(7520), 80–83. <https://doi.org/10.1038/nature13796>
- Åström, J. A., Cook, S., Enderlin, E. M., Sutherland, D. A., Mazur, A., & Glasser, N. (2021). Fragmentation theory reveals processes controlling iceberg size distributions. *Journal of Glaciology*, 67(264), 603–612. <https://doi.org/10.1017/jog.2021.14>
- Åström, J. A., Riikilä, T. I., Tallinen, T., Zwinger, T., Benn, D., Moore, J. C., & Timonen, J. (2013). A particle based simulation model for glacier dynamics. *The Cryosphere*, 7(5), 1591–1602. <https://doi.org/10.5194/tc-7-1591-2013>
- Åström, J. A., Vallot, D., Schäfer, M., Welty, E. Z., O’Neel, S., Bartholomaus, T. C., et al. (2014). Termini of calving glaciers as self-organized critical systems. *Nature Geoscience*, 7(12), 874–878. <https://doi.org/10.1038/NGEO2290>
- Bassis, J., & Jacobs, S. (2013). Diverse calving patterns linked to glacier geometry. *Nature Geoscience*, 6(10), 833–836. <https://doi.org/10.1038/geo1887>
- Blatny, L., Löwe, H., & Gaume, J. (2023). Microstructural controls on the plastic consolidation of porous brittle solids. *Acta Materialia*, 250, 118861. <https://doi.org/10.1016/j.actamat.2023.118861>
- Blatny, L., Löwe, H., Wang, S., & Gaume, J. (2021). Computational micromechanics of porous brittle solids. *Computers and Geotechnics*, 140, 104284. <https://doi.org/10.1016/j.compgeo.2021.104284>
- Chudley, T. R., Christoffersen, P., Doyle, S. H., Dowling, T. P. F., Law, R., Schoonman, C. M., et al. (2021). Controls on water storage and drainage in crevasses on the Greenland ice sheet. *Journal of Geophysical Research: Earth Surface*, 126(9), e2021JF006287. <https://doi.org/10.1029/2021JF006287>
- Colgan, W., Rajaram, H., Abdalati, W., McCutchan, C., Mottram, R., Moussavi, M. S., & Grigsby, S. (2016). Glacier crevasses: Observations, models, and mass balance implications. *Reviews of Geophysics*, 54(1), 119–161. <https://doi.org/10.1002/2015RG000504>
- Duddu, R., Jiménez, S., & Bassis, J. (2020). A non-local continuum poro-damage mechanics model for hydrofracturing of surface crevasses in grounded glaciers. *Journal of Glaciology*, 66(257), 415–429. <https://doi.org/10.1017/jog.2020.16>
- Duddu, R., & Waisman, H. (2013). A nonlocal continuum damage mechanics approach to simulation of creep fracture in ice sheets. *Computational Mechanics*, 51(6), 961–974. <https://doi.org/10.1007/s00466-012-0778-7>

- Enderlin, E. M., & Bartholomaus, T. C. (2020). Sharp contrasts in observed and modeled crevasse patterns at Greenland's marine terminating glaciers. *The Cryosphere*, 14(11), 4121–4133. <https://doi.org/10.5194/tc-14-4121-2020>
- Gans, A., Abramian, A., Lagrée, P.-Y., Gong, M., Sauret, A., Pouliquen, O., & Nicolas, M. (2023). Collapse of a cohesive granular column. *Journal of Fluid Mechanics*, 959, A41. <https://doi.org/10.1017/jfm.2023.180>
- Garvin, J. B., & Williams, R. S. (1993). Geodetic airborne laser altimetry of Breidamerkurjökull and Skeidararárjökull, Iceland, and Jakobshavn Isbræ, West Greenland. *Annals of Glaciology*, 17, 379–385. <https://doi.org/10.3189/s0260305500013136>
- Gaume, J., Gast, T., Teran, J., van Herwijnen, A., & Jiang, C. (2018). Dynamic anticrack propagation in snow. *Nature Communications*, 9(4), 3047. <https://doi.org/10.1038/s41467-018-05181-w>
- Guillet, L., Blatny, L., Trottet, B., Steffen, D., & Gaume, J. (2023). A depth-averaged material point method for shallow landslides: Applications to snow slab avalanche release. *Journal of Geophysical Research: Earth Surface*, 128(8), e2023JF007092. <https://doi.org/10.1029/2023JF007092>
- Herzfeld, U. C., Trantow, T., Lawson, M., Hans, J., & Medley, G. (2021). Surface heights and crevasse morphologies of surging and fast-moving glaciers from ICESat-2 laser altimeter data - application of the density-dimension algorithm (DDA-ice) and evaluation using airborne altimeter and Planet SkySat data. *Science of Remote Sensing*, 3, 100013. <https://doi.org/10.1016/j.srs.2020.100013>
- Holdsworth, G. (1969). Primary transverse crevasses. *Journal of Glaciology*, 8(52), 107–129. <https://doi.org/10.3189/S0022143000020797>
- Huth, A., Duddu, R., & Smith, B. (2021a). A generalized interpolation material point method for shallow ice shelves. 1: Shallow shelf approximation and ice thickness evolution. *Journal of Advances in Modeling Earth Systems*, 13(8). <https://doi.org/10.1029/2020MS002277>
- Huth, A., Duddu, R., & Smith, B. (2021b). A generalized interpolation material point method for shallow ice shelves. 2: Anisotropic nonlocal damage mechanics and rift propagation. *Journal of Advances in Modeling Earth Systems*, 13(8). <https://doi.org/10.1029/2020MS002292>
- Jiménez, S., & Duddu, R. (2018). On the evaluation of the stress intensity factor in calving models using linear elastic fracture mechanics. *Journal of Glaciology*, 64(247), 759–770. <https://doi.org/10.1017/jog.2018.64>
- Jóhannesson, T., Thorsteinsson, T., Stefánsson, A., Gaidos, E. J., & Einarrson, B. (2007). Circulation and thermodynamics in a subglacial geothermal lake under the Western Skáftá cauldron of the Vatnajökull ice cap, Iceland. *Geophysical Research Letters*, 34(19). <https://doi.org/10.1029/2007GL030686>
- Klár, G., Gast, T., Pradhana, A., Fu, C., Schroeder, C., Jiang, C., & Teran, J. (2016). Drucker-prager elastoplasticity for sand animation. *ACM Transactions on Graphics*, 35(4), 1–12. <https://doi.org/10.1145/2897824.2925906>
- Kohler, M., Stoecklin, A., & Puzrin, A. M. (2022). A MPM framework for large-deformation seismic response analysis. *Canadian Geotechnical Journal*, 59(6), 1046–1060. <https://doi.org/10.1139/cgj-2021-0252>
- Kozioł, C. P., & Arnold, N. (2018). Modelling seasonal meltwater forcing of the velocity of land-terminating margins of the Greenland ice sheet. *The Cryosphere*, 12(3), 971–991. <https://doi.org/10.5194/tc-12-971-2018>
- Krug, J., Weiss, J., Gagliardini, O., Gagliardini, O., & Durand, G. (2014). Combining damage and fracture mechanics to model calving. *The Cryosphere*, 8(6), 2101–2117. <https://doi.org/10.5194/tc-8-2101-2014>
- Magnússon, E., Pálsson, F., Guðmundsson, M. T., Högnadóttir, T., Rossi, C., Thorsteinsson, T., et al. (2021). Development of a subglacial lake monitored with radio-echo sounding: Case study from the eastern Skáftá cauldron in the Vatnajökull ice cap, Iceland. *The Cryosphere*, 15(8), 3731–3749. <https://doi.org/10.5194/tc-15-3731-2021>
- Malthe-Sørensen, A., Walmann, T., Jamtveit, B., Feder, J., & Jøssang, T. (1999). Simulation and characterization of fracture patterns in glaciers. *Journal of Geophysical Research: Solid Earth*, 104(B10), 23157–23174. <https://doi.org/10.1029/1999JB900219>
- Mast, C. M. (2013). *Modeling landslide-induced flow interactions with structures using the material point method*. (PhD thesis). University of Washington
- McGrath, D., Colgan, W., Steffen, K., Lauffenburger, P., & Balog, J. (2011). Assessing the summer water budget of a moulin basin in the sermeq avannarleq ablation region, Greenland ice sheet. *Journal of Glaciology*, 57(205), 954–964. <https://doi.org/10.3189/002214311798043735>
- Mottram, R. H., & Benn, D. I. (2009). Testing crevasse-depth models: A field study at Breidamerkurjökull, Iceland. *Journal of Glaciology*, 55(192), 746–752. <https://doi.org/10.3189/002214309789747095>
- Nielsen, L. E. (1958). Crevasse patterns in glaciers. *The American Alpine Journal*, 11, 44–51.
- Nye, J. F. (1955). Comments on Dr. Loewe's letter and notes on crevasses. *Journal of Glaciology*, 2(17), 512–514. <https://doi.org/10.3189/s002214300032652>
- Nye, J. F. (1957). The distribution of stress and velocity in glaciers and ice-sheets. *Proceedings of the Royal Society of London - Series A: Mathematical and Physical Sciences*, 239(1216), 113–133.
- Petrenko, V., & Whitworth, R. (1999). *Physics of ice*. OUP.
- Phillips, T., Rajaram, H., & Steffen, K. (2010). Cryo-hydrologic warming: A potential mechanism for rapid thermal response of ice sheets. *Geophysical Research Letters*, 37(20). <https://doi.org/10.1029/2010GL044397>
- Pralong, A., & Funk, M. (2005). Dynamic damage model of crevasse opening and application to glacier calving. *Journal of Geophysical Research: Solid Earth*, 110(B1). <https://doi.org/10.1029/2004JB003104>
- Pralong, A., Funk, M., & Lüthi, M. P. (2003). A description of crevasse formation using continuum damage mechanics. *Annals of Glaciology*, 37, 77–82. <https://doi.org/10.3189/172756403781816077>
- Rousseau, H., Gaume, J., Blatny, L., & Lüthi, M. P. (2024). Data supporting "Transition between mechanical and geometric controls in glacier crevassing processes". Zenodo. <https://doi.org/10.5281/zenodo.10451296>
- Schoof, C. (2010). Ice-sheet acceleration driven by melt supply variability. *Nature*, 468(7325), 803–806. <https://doi.org/10.1038/nature09618>
- Simo, J. C. (1992). Algorithms for static and dynamic multiplicative plasticity that preserve the classical return mapping schemes of the infinitesimal theory. *Computer Methods in Applied Mechanics and Engineering*, 99(1), 61–112. [https://doi.org/10.1016/0045-7825\(92\)90123-2](https://doi.org/10.1016/0045-7825(92)90123-2)
- Smith, R. (1976). The application of fracture mechanics to the problem of crevasse penetration. *Journal of Glaciology*, 17(76), 223–228. <https://doi.org/10.3189/s0022143000013563>
- Sole, A. J., Mair, D. W. F., Nienow, P. W., Bartholomew, I. D., King, M. A., Burke, M. J., & Joughin, I. (2011). Seasonal speedup of a Greenland marine-terminating outlet glacier forced by surface melt-induced changes in subglacial hydrology. *Journal of Geophysical Research*, 116(F3), F03014. <https://doi.org/10.1029/2010JF001948>
- Stomakhin, A., Schroeder, C., Chai, L., Teran, J., & Selle, A. (2013). A material point method for snow simulation. *ACM Transactions on Graphics*, 32(4), 1–10. <https://doi.org/10.1145/2461912.2461948>
- Sulsky, D., Chen, Z., & Schreyer, H. (1994). A particle method for history-dependent materials. *Computer Methods in Applied Mechanics and Engineering*, 118(1), 179–196. [https://doi.org/10.1016/0045-7825\(94\)90112-0](https://doi.org/10.1016/0045-7825(94)90112-0)
- Ultee, L., Meyer, C., & Minchew, B. (2020). Tensile strength of glacial ice deduced from observations of the 2015 eastern Skáftá cauldron collapse, Vatnajökull ice cap, Iceland. *Journal of Glaciology*, 66(260), 1024–1033. <https://doi.org/10.1017/jog.2020.65>

- van der Veen, C. (1998). Fracture mechanics approach to penetration of bottom crevasses on glaciers. *Cold Regions Science and Technology*, 27(3), 213–223. [https://doi.org/10.1016/s0165-232x\(98\)00006-8](https://doi.org/10.1016/s0165-232x(98)00006-8)
- van der Veen, C. (1999). Crevasses on glaciers. *Polar Geography*, 23(3), 213–245. <https://doi.org/10.1080/10889379909377677>
- van der Veen, C. J. (2007). Fracture propagation as means of rapidly transferring surface meltwater to the base of glaciers. *Geophysical Research Letters*, 34(1). <https://doi.org/10.1029/2006GL028385>
- Vaughan, D. G. (1995). Tidal flexure at ice shelf margins. *Journal of Geophysical Research*, 100(B4), 6213–6224. <https://doi.org/10.1029/94JB02467>
- Walter, A., Lüthi, M. P., & Vieli, A. (2020). Calving event size measurements and statistics of Eqip Sermia, Greenland, from terrestrial radar interferometry. *The Cryosphere*, 14(3), 1051–1066. <https://doi.org/10.5194/tc-14-1051-2020>
- Weertman, J. (1977). Penetration depth of closely spaced water-free crevasses. *Journal of Glaciology*, 18(78), 37–46. <https://doi.org/10.3189/S0022143000021493>
- Weiss, J. (2003). Scaling of fracture and faulting of ice on Earth. *Surveys in Geophysics*, 24(4), 185–227. <https://doi.org/10.1023/A:1023293117309>
- Weiss, J. (2019). Ice: The paradigm of wild plasticity. *Philosophical Transactions of the Royal Society A: Mathematical, Physical & Engineering Sciences*, 377(2146), 20180260. <https://doi.org/10.1098/rsta.2018.0260>
- Wolper, J., Fang, Y., Li, M., Lu, J., Gao, M., & Jiang, C. (2019). Cd-mpm: Continuum damage material point methods for dynamic fracture animation. *ACM Transactions on Graphics*, 38(4), 1–15. <https://doi.org/10.1145/3306346.3322949>
- Wolper, J., Gao, M., Lüthi, M. P., Heller, V., Vieli, A., Jiang, C., & Gaume, J. (2021). A glacier–ocean interaction model for tsunami genesis due to iceberg calving. *Communications Earth & Environment*, 2(1), 1–10. <https://doi.org/10.1038/s43247-021-00179-7>
- Zhang, H., Davis, T., Katz, R. F., Stevens, L. A., & May, D. A. (2023). Basal hydrofractures near sticky patches. *Journal of Glaciology*, 69(275), 475–486. <https://doi.org/10.1017/jog.2022.75>

Erratum

The originally published version of this article omitted the supporting information movie files. The error has been corrected, and this may be considered the authoritative version of record.